Available online at www.sciencedirect.com
ScienceDirect
Journal of Power Sources 166 (2007) 386–399
JOURNAL OF POWER SOURCES
www.elsevier.com/locate/jpowsour

Modelling of a cathode-supported tubular solid oxide fuel cell operating with biomass-derived synthesis gas

R. Suwanwarangkul [a], E. Croiset [b,*], M.D. Pritzker [b], M.W. Fowler [b], P.L. Douglas [b], E. Entchev [c]

[a] *School of Bio-Chemical Engineering and Technology, Sirindhorn International Institute of Technology, Thammasart University-Rangsit Campus, Pathum Thani 12121, Thailand*
[b] *Department of Chemical Engineering, University of Waterloo, Waterloo, Ont. N2L 3G1, Canada*
[c] *Advance Combustion Technologies Laboratory, CANMET Energy Technology Centre, 1 Haanel Drive, Ottawa, Ont. K1A 1M1, Canada*

Received 23 October 2006; received in revised form 22 December 2006; accepted 22 December 2006
Available online 17 January 2007

Abstract

A mechanistic model for the operation of a tubular solid oxide fuel cell (SOFC) using synthesis gas as a fuel source has been successfully developed and validated against experimental data reported in the literature. The model considers momentum-, mass-, energy- and charge-transport equations coupled with electrochemical and water-gas shift reactions. This avoids the use of empirical correlations for estimating heat and mass transfer coefficients. The model is solved to predict SOFC performance and behavior by determining the distributions of current density, temperature and species concentrations throughout the cell. The developed model was used to predict the effect of the composition of biomass-derived synthesis gas fuels on cell performance and behavior.

Keywords: Mechanistic modelling; Tubular SOFC; Cathode-supported; Synthesis gas; Biomass fuel

1. Introduction

Heat engines that are widely employed to produce electricity and heat for homes and industries have relatively low energy efficiency and emit large amounts of greenhouse gases. Tubular solid oxide fuel cells (TSOFC) show great promise as potential candidates to replace conventional heat engines. TSOFCs have, indeed, higher energy efficiency and emit lower amounts of greenhouse gases. Furthermore, they are designed for mid- to large-scale applications up to 2 MW [1], similar to the capacity of heat engines. A major advantage of TSOFCs over other types of fuel cells is that a variety of hydrocarbon-based gases or their synthesis derivatives, such as natural gas, biomass and coal can potentially be used as fuel sources. CO present in the synthesis gas can be oxidized in TSOFCs to generate CO_2 and electrical energy.

Recently, the use of biomass-derived synthesis gas as a fuel has gained attention because it is abundant and renewable. Omosun et al. [2] performed a system analysis on a SOFC combined with biomass gasification. The biomass was gasified in air yielding a syngas composition of 17% H_2, 13% CO, 11% CO_2, 4% CH_4, 15% H_2O and 40% N_2. A simple SOFC model developed in gPROMS accounted only for the electrochemical oxidation of H_2 and the consumption of CO via the water-gas shift (WGS) reaction. In addition to presenting the overall model, the main objective of this paper was to compare cleanup of hot gas to that of cold gas. Panopoulos et al. [3] also carried out a system analysis of an SOFC integrated with a biomass steam gasification process. The resulting humidified syngas had the following composition: 26.2% H_2, 15.9% CO, 6.0% CO_2, 2.6% CH_4 and 49.1% H_2O. The SOFC model was a simple equilibrium model developed in AspenPlus. Cordiner et al. [4] simulated a biomass gasifier coupled with an SOFC. The gasification process was considered to be at equilibrium whereas they developed a 3D model for a single planar SOFC. The composition of the syngas leaving the gasifier and fed to the SOFC was 56% H_2, 39% CO and 6% CO_2. In their SOFC model, only the electrochemical

* Corresponding author. Tel.: +1 519 888 4567x36472; fax: +1 519 746 4979.
E-mail address: ecroiset@cape.uwaterloo.ca (E. Croiset).

0378-7753/$ – see front matter © 2007 Elsevier B.V. All rights reserved.
doi:10.1016/j.jpowsour.2006.12.096

oxidation of H_2 was considered and CO was consumed only via the WGS reaction. They determined that the whole system had an efficiency close to 46%. Aloui and Halouani [5] developed an isothermal 1D model for an SOFC fed by biomass syngas that considered the electrochemical oxidation of both CO and H_2. A somewhat surprising result of their analysis was that biomass syngas (26% H_2, 24% CO, balance mostly N_2) yielded better performance than diluted humidified hydrogen (49% H_2, 1.5% H_2O, 46% N_2, balance CO and CO_2). It is difficult to assess this result more deeply especially since it was unclear whether the water-gas shift reaction was taken into account.

Van Herle et al. [6–8] investigated a slightly different system from the previously described works in that the fuel fed to the SOFC was a biogas reformate instead of biomass-gasified syngas. The composition of this reformate was 35.8% H_2, 29.6% CO, 3.6% CO_2, 0.2% CH_4, 4.3% H_2O and 26.5% N_2. Van Herle et al. developed a flowsheet for the entire system, including the biogas reformer, where the SOFC was simulated using a simplified isothermal model. Vasileiadis and Ziaka-Vasileiadou [9] also considered reforming of biogas prior to an SOFC. They focused more on the reformer and very little detail was given regarding the SOFC. Very recently, a biogas reformer/SOFC system was also investigated by Athanasioua et al. [10]. The composition of the biogas reformate fed to the SOFC was 19% H_2, 11% CO, 5% CO_2, 1% CH_4, 23% H_2O and 43% N_2. Their model was equilibrium based with the assumption of 80% CO utilization.

Although not involving model simulation, a noteworthy study on the use of biomass syngas in SOFC was the work of Xie et al. [11] who experimentally investigated the performance of a Ni–Cu alloy-based anode for low temperature SOFCs. The fuel used was a syngas produced from rice husk gasification (23.5% CO, 14.3% CO_2, 15.7% H_2, 6.2% CH_4 and 40.3% N_2). Their main conclusion was that the Ni–Cu alloy system was more stable than the Ni one because of significant reduction in carbon deposition due to the replacement of Ni by Cu. Baron et al. [12] also studied experimentally the effect of various simulated biomass gas compositions on the cell performance at an intermediate temperature of 650 °C. They found that the performance of the cell decreased at a CH_4 content of 10%. They also observed that replacing H_2 by CO had a negative impact on the cell performance, which they attributed mostly to differences in mass-transport properties between CO and H_2. This latter conclusion was also reached by Suwanwarangkul et al. [13] for higher temperature cells. Aravind et al. [14] also conducted experiments on the cell performance using Ni/GDC and SDC anodes for different types of biosyngas (air-blown, oxygen-blown and steam gasification) at operating temperatures between 750 and 1000 °C. For the syngas compositions they considered, they observed no significant carbon deposition, as expected from C–H–O ternary diagrams. Interestingly, they also performed experiments where 9 ppm H_2S was added to the simulated biogas (but only with the Ni/GDC anode) and observed no deleterious effects. One should note, however, that 9 ppm H_2S is below the level that would be expected in biosyngas (50–200 ppm [14]). Several studies on the direct use of biogas in SOFC have also been reported [15,16].

As just described, only a limited amount of research has been done to study the use of biomass-derived synthesis gas as a fuel source. Furthermore, the studies to date have focused mostly on system analysis and anode material development. No work has been found on the application of a mechanistic model to an actual tubular cell operating with a biomass-derived syngas. Since the composition of synthesis gas can vary widely depending on the biomass type and gasification process [17], there is an important need to develop mathematical models to predict the effect of fuel composition and other operating conditions on cell performance indicators such as power output, efficiency and outlet gas temperature and composition. In addition, such models can be used to study the complex interactions between physical phenomena and reaction processes (chemical/electrochemical) that take place in a TSOFC and are critical to optimize the cell performance and to help in designing the cell.

TSOFC models that have been recently developed have been reviewed by Suwanwarangkul [18]. The TSOFC models have so far focused almost exclusively on the use of H_2 [19,20], methane [21,22], and natural gas and pre-reformed natural gas [23–26]. One exception is a study on pre-reformed jet fuel in TSOFC [27]. In all the above models for TSOFC, the equilibrium of the WGS reaction was assumed. Also, with the exception of the work of Aguiar et al. [22], consumption of CO via the WGS reaction was considered, but not its electrochemical oxidation. On the other hand, Li and Chyu [25] showed that the Nernst potentials for CO and H_2 electrochemical oxidation are the same as long as the WGS equilibrium is assumed. They concluded that it is sufficient to consider H_2 oxidation to be the only anodic reaction if it is coupled to the consumption of CO via the WGS reaction at pseudo-equilibrium. Although it is generally accepted that the WGS reaction is fast and quickly reaches equilibrium at the temperatures encountered in an SOFC, this has not been firmly demonstrated and it is not clear yet whether this assumption would still be valid when a syngas containing a high concentration of CO is fed to the cell. One of the objectives of the present study is to test this assumption. Consequently, we make no assumption regarding the equilibrium of the WGS reaction in the model to be considered and so also explicitly include the electrochemical oxidation of CO. The main difference between our model and the TSOFC models described above is that the WGS reaction is not assumed to be at equilibrium *a priori* and therefore the inclusion of CO electrochemical oxidation is necessary in our model. Since biogas is composed essentially of CO_2 and CH_4, dry and steam reforming of methane would also become major reactions occurring in the SOFC. However, we do not consider methane reforming in the model to be presented and thus the results will be most relevant to the use of biomass-derived syngas.

In the present work, a comprehensive mathematical model of a TSOFC presented in detail in earlier publications [13,19] was used to simulate a TSOFC operating with biomass-derived syngas. The model aims at predicting such quantities as the current density and temperature distributions throughout the cell for different compositions of the fuel gas. Fuel gases considered in the model are humidified hydrogen and synthesis gas (mixtures of H_2, H_2O, CO, CO_2 and N_2) while the oxidant

is air. The model domains include the air channel, fuel channel, electrochemical cell and the air-preheating tube. The model is composed of momentum-, heat-, mass- and charge-transport equations coupled with the electrochemical and water-gas shift reactions. Consequently, the use of empirical correlations for heat and mass transfer is avoided. Radiative heat transfer is also incorporated into the model to account for heat transfer from the cell to the air-preheating tube. The model is validated against experimental data for an operating TSOFC reported in the literature. Once validated, the model is used to explore the effect of fuel gas composition on cell performance and the implications for successful fuel cell operation.

2. Mathematical modelling

2.1. Model setup and assumptions

Since the details of the model used in this paper were presented previously [13,19], only its main features are reported here, as well as some equations specific to syngas operation in a TSOFC not reported previously.

The geometry of a TSOFC within a stack is similar to that presented by Suwanwarangkul et al. [19] and is shown in Fig. 1. Due to symmetry of the cell geometry, only the half portion on one side of the central axis has to be considered in the model (Fig. 2).

Regarding TSOFC operation, air, already at approximately 600 °C before entering the cell, is further heated as it passes through an air-preheating tube located in the center of the tubular cell. The heat source for air preheating comes from the exothermic electrochemical cell reactions. Once the air reaches the closed end of the tube, it enters the annular air channel between the outer side of the air-preheating tube and the inner side of the cathode and begins to flow in the reverse direction. Oxygen diffuses through the thick porous cathode and reaches the active sites at the cathode/electrolyte interface where the following reduction reaction takes place to produce O^{2-}:

$$O_2 + 4e^- \rightarrow 2O^{2-} \quad (1)$$

The O^{2-} ions are conducted through the electrolyte from the cathode to active anode sites at the anode/electrolyte interface. Simultaneously, the synthesis gas is supplied from the outside of the cell along the cell length. Since nickel used in the anode is a good catalyst for the water-gas shift (WGS) and carbon formation reactions (e.g. Boudouard reaction), H_2, and eventually carbon, are produced on the anode surface via the following reactions:

$$CO + H_2O \rightleftharpoons CO_2 + H_2 \quad \text{(WGS)} \quad (2)$$

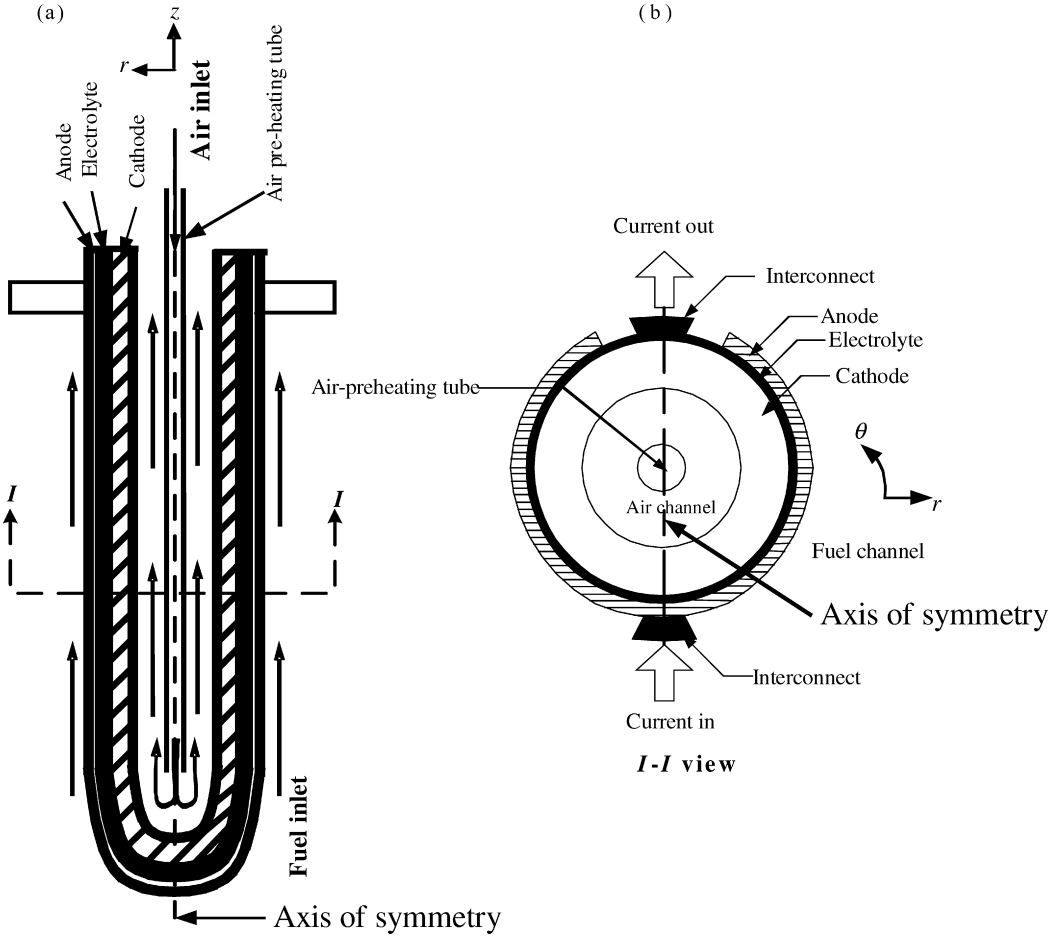

Fig. 1. Schematic diagram of a TSOFC: (a) longitudinal and (b) cross-sectional sections of the cell.

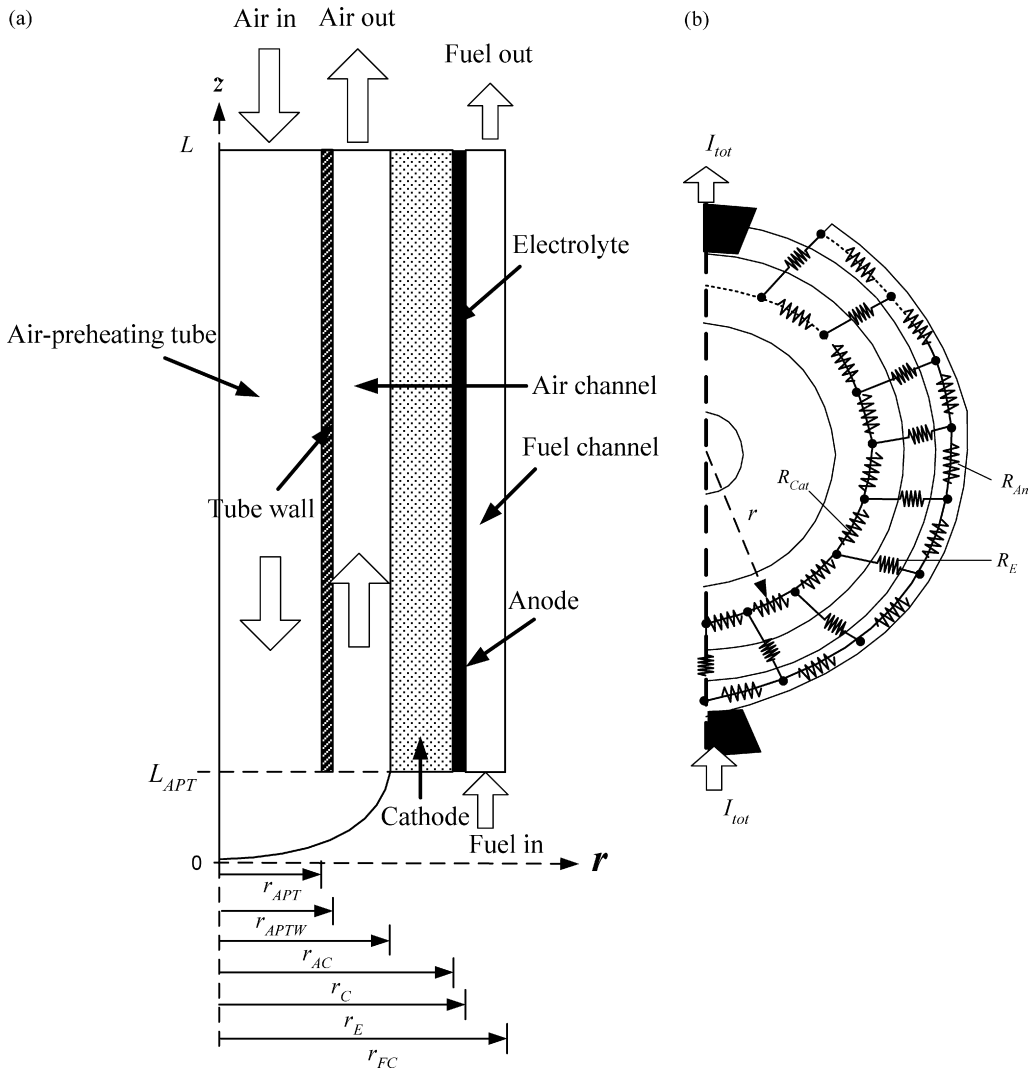

Fig. 2. TSOFC geometry considered in the model showing the half portions of: (a) longitudinal and (b) cross-sectional sections of the cell. Not to scale.

$$2CO \rightleftharpoons C + CO_2 \quad \text{(Boudouard)} \tag{3}$$

Thereafter, H_2 and CO in the synthesis gas diffuse through the thin porous anode and electrochemically react with O^{2-} at the anode active sites to produce H_2O and CO_2 which diffuse back into the fuel stream and are removed together with the unreacted fuel. The oxidation reactions occurring in SOFCs are as follows

$$H_2 + O^{2-} \rightarrow H_2O + 2e^- \tag{4}$$

$$CO + O^{2-} \rightarrow CO_2 + 2e^- \tag{5}$$

The objective of the model is to determine the distributions of velocity, temperature, species concentrations, current density and ionic potential in the flow passages and/or cell structure within the longitudinal section of the cell (Fig. 2a). Therefore, the momentum-, heat-, mass- and charge-transport equations coupled with electrochemical and chemical reactions are governed by this geometry. The ohmic overpotentials due to current flows along the peripheral paths within the anode and the cathode are estimated using the equivalent circuit shown in Fig. 2b for the electrical resistance within the cross-sectional area of the cell. As previously presented by Suwanwarangkul et al. [19], this analysis allows the ohmic overpotentials in the cathode ($\eta_{Ohm,Cat}$) and in the anode ($\eta_{Ohm,An}$) to be determined as a function of the current density J_{tot} generated within the cell. These relationships were shown to be largely independent of temperature under typical operating conditions since the electrode resistance does not vary much over the range 800 to 1200 °C.

The ohmic overpotentials were estimated to be [19]:

$$\eta_{Ohm,Cat} = 1.2 \times 10^{-5} J_{avg} \tag{6}$$

$$\eta_{Ohm,An} = 3.9 \times 10^{-6} J_{avg} \tag{7}$$

Model assumptions simplify the complexity of the system while still maintaining features required to accurately describe the operation of a TSOFC. They are listed as follows:

- The model is based on steady-state, non-isothermal operation using synthesis gas as the fuel source (mixtures of H_2, CO, CO_2, H_2O and N_2).
- The fuel cell operates with 100% current efficiency, i.e. no reactant gas crossover or side reactions occur.

- Ideal gas law is assumed for all species components.
- Gas flow in the air channel is laminar.
- Plug-flow conditions are assumed in the fuel channel. Therefore, the gas temperature and species concentrations change only in the z-direction.
- The gas velocity is assumed to be uniform throughout the fuel channel and consequently the momentum equation was not considered for the fuel channel.
- Radiative heat transfer occurs only between the air-preheating tube and cell structure.
- Heat- and mass-transport limitations at the anode are neglected because of the thin anode layer. For further simplification, it was assumed that the anode has zero thickness.
- Heat transport within the porous cathode occurs only by conduction.
- No carbon formation reaction takes place at the anode.

The assumption concerning uniform gas velocity along the fuel channel is justified as follows. The variation in gas velocity along the fuel channel is due primarily to changes in temperature and gas composition. For a fuel inlet temperature of 800 °C, a temperature increase through the fuel channel of 200 °C (typical of the maximum temperature increase found for biomass syngas operation, as shown later) decreases the gas density by 19% and therefore only moderately increases the gas velocity. In addition, this change in gas velocity due to temperature increase is counterbalanced by the formation of heavier molecules through the reactions of H_2 to H_2O and CO to CO_2. The conversion of CO to CO_2 will only have a modest effect on the gas velocity since the molecular weight of CO_2 is only 1.57 times that of CO. The conversion of H_2 to H_2O, on the other hand, has a more pronounced impact on the gas velocity due to the much larger difference in molecular weight between H_2 and H_2O. In the case of a syngas where the concentration of H_2 is not too high (15–40%), we conducted detailed simulations that included the momentum balance in the fuel channel and obtained only small differences from the situation where uniform gas velocity was assumed. Inclusion of the momentum balance for the $H_2/CO/H_2O/CO_2$ mixture greatly increased the computation time without a significant difference in results. Consequently, we chose to assume uniform gas velocity in the fuel channel.

The model considers the electrochemical oxidation of both CO and H_2. It also takes into account the water-gas shift reaction, but without assuming that it is at equilibrium. As noted previously, the model does not include methane reforming since it is assumed here that the mixture fed to the SOFC contains little or no methane. Most governing equations have been reported in our previous studies [13,19], except for the fuel channel where the steady-state material balance for each species is

$$\frac{\partial(c_i v_f)}{\partial z} + \frac{1}{r}\frac{\partial(r c_i u_f)}{\partial r} = \frac{\partial}{\partial z}\left(D_{i\text{-M}}\frac{\partial c_i}{\partial z}\right) + \frac{1}{r}\frac{\partial}{\partial r}\left(r D_{i\text{-M}}\frac{\partial c_i}{\partial r}\right) \quad (8)$$

where c_i is the molar concentration of a fuel gas species ($i = H_2$, H_2O and CO), $D_{i\text{-M}}$ the binary diffusion coefficient of ith species in the mixture and u_f, v_f are the fuel velocities. c_{CO_2} can be determined by

$$c_{CO_2} = c_{tot,f} - c_{H_2} - c_{CO} - c_{CO_2} - c_{N_2}$$

where c_{tot} is the total concentration.

The momentum-, mass- and energy-transport equations are solved simultaneously within the air-preheating tube, air channel and porous cathode to determine the concentration, velocity and temperature profiles. The mass transport of O_2 inside the thick porous cathode is determined using the dusty-gas model since it has been shown to accurately predict the concentration overpotential in comparison to the Fick and Stefan–Maxwell models [28]. The charge-transport equation is employed to determine the O^{2-} distribution within the electrolyte and to estimate the ohmic overpotential in the electrolyte. In the fuel channel, momentum transport is neglected as discussed previously. Accordingly, this leads to the conditions $v_f = v_{f,in}$, $u_f = 0$ and $p_f = p_{f,in}$ where v_f, u_f and p_f denote the fuel velocity in the axial direction, fuel velocity in the radial direction and fuel pressure, respectively.

2.2. Boundary conditions

The boundary regions used to solve the governing equations are based on Fig. 2a. The species concentrations and temperatures are prescribed at the gas inlet regions (i.e. $z = L_{APT}$, $r_E < r < r_{FC}$ for the fuel, and $z = L$, $0 < r < r_{APT}$ for air). The air velocity is specified at the inlet of the air-preheating tube. At the gas outlet regions (i.e. $z = L$, $r_E < r < r_{AC}$ and $z = L$, $r_{APTW} < r < r_{FC}$), only the outlet air pressure is specified (i.e. $p_a = 1.1035 \times 10^5$ Pa); the gradients or fluxes of all other variables in the flow direction are zeros (i.e. $\partial u_a/\partial z = 0$, $\partial v_a/\partial z$, $\partial T_{a,f}/\partial z = 0$ and $\partial c_{a,f}/\partial z = 0$). Along the symmetrical z-axis of the air-preheating tube and fuel channel, the fluxes or gradients normal to the boundary regions are zero, i.e. $\partial T_{a,f}/\partial r = 0$, $\partial c_{O_2}/\partial r = 0$ and $\partial v_a/\partial r = 0$ and $u_a = 0$. At the closed end, $u_a = 0$, $v_a = 0$, $T = T_{f,in}$ and $\nabla c_{O_2}(r, z) = 0$.

At the fuel channel/electrolyte interface, i.e. ($L_{APT} < z < L$, $r = r_E$), the electrochemical oxidation of H_2 and CO are assumed to take place because the anode thickness is neglected. Furthermore, O_2 reduction takes place at the cathode/electrolyte interface, i.e. ($L_{APT} < z < L$, $r = r_C$). The boundary conditions used at these interfaces to solve the mass-, energy- and charge-transport equations are summarized in Table 1. $Q_{electrochem}$ and Q_{WGSR} denote the heat generation due to the electrochemical

Table 1
Boundary conditions at the fuel channel/electrolyte (FC/E) and cathode/electrolyte (C/E) interfaces used to solve the mass-, energy- and charge-transport equations

Transport equation	Boundary conditions at the electrode/electrolyte interfaces	
	FC/E ($L_{APT} < z < L$, $r = r_E$)	C/E ($L_{APT} < z < L$, $r = r_C$)
Species	$\mathbf{n}\cdot\vec{N}_{H_2} = -J_{H_2}/2F + R_{WGR}$ $\mathbf{n}\cdot\vec{N}_{CO} = -J_{CO}/2F - R_{WGR}$ $\mathbf{n}\cdot\vec{N}_{H_2O} = J_{H_2}/2F - R_{WGR}$	$\mathbf{n}\cdot\vec{m}_{O_2} = -M_{O_2} J_{O_2}/4F$
Energy	$\mathbf{n}\cdot\vec{q}_{Cond} = Q_{electrochem} + Q_{WGSR}$	$\mathbf{n}\cdot\vec{q}_{Cond,E} = \mathbf{n}\cdot\vec{q}_{Cond,Cat}$
Charge	$\mathbf{n}\cdot\vec{i} = J_{H_2} + J_{CO}$	$\mathbf{n}\cdot\vec{i} = -J_{O_2}$

and water-gas shift reactions, respectively, while $\vec{N}_i$, $\vec{m}_{O_2}$, $\vec{q}_{Cond}$ and $\vec{i}$ are the molar flux of a fuel gas species ($i = H_2$, H_2O and CO), mass flux of O_2, conductive heat flux and charge flux, respectively. $Q_{electrochem}$ is calculated as the difference between the total power generated by the electrochemical reactions and the electrical power delivered by the cell, i.e.,

$$Q_{electrochem} = \left(\frac{-J_{H_2}}{2F}\right)\Delta H_{r\times n,H_2} + \left(\frac{-J_{CO}}{2F}\right)\Delta H_{r\times n,CO} - (J_{H_2} + J_{CO})(\phi_{Cat} - \phi_{An}) \quad (9)$$

where $\Delta H_{r\times n,H_2}$ and $\Delta H_{r\times n,CO}$ are the enthalpies of reaction for the overall electrochemical oxidation of H_2 ($H_2 + (1/2)O_2 \rightarrow H_2O$) and CO ($CO + (1/2)O_2 \rightarrow CO_2$), respectively. ϕ_{An} and ϕ_{Cat} are the electrode potentials at the anode and cathode interconnect plates, respectively.

Q_{WGSR} is estimated as

$$Q_{WGSR} = R_{WGSR}\Delta H_{r\times n,WGSR} \quad (10)$$

where $\Delta H_{r\times n,WGSR}$ is the enthalpy of reaction for the WGR calculated as

$$\Delta H_{r\times n,WGSR} = \Delta H_{f,H_2} + \Delta H_{f,CO_2} - \Delta H_{f,CO} - \Delta H_{f,H_2O} \quad (11)$$

Due to the radiative heat exchange between the surface of the cathode ($L_{APT} < z < L$, $r = r_{AC}$) and that of the air-preheating tube ($L_{APT} < z < L$, $r = r_{APTW}$), the following boundary conditions apply: $\mathbf{n}\cdot(\lambda_{Cat}\nabla T) = -\sigma_0 F_r(T^4|_{r=r_{AC}} - T^4|_{r=r_{APTW}})$ at $L_{APT} < z < L$ and $r = r_{AC}$ and $\mathbf{n}\cdot(\lambda_{APT}\nabla T) = \sigma_0 F_r(T^4|_{r=r_{AC}} - T^4|_{r=r_{APTW}})$ at $L_{APT} < z < L$, $r = r_{APTW}$, where F_r is the correction factor for heat radiation [19,29].

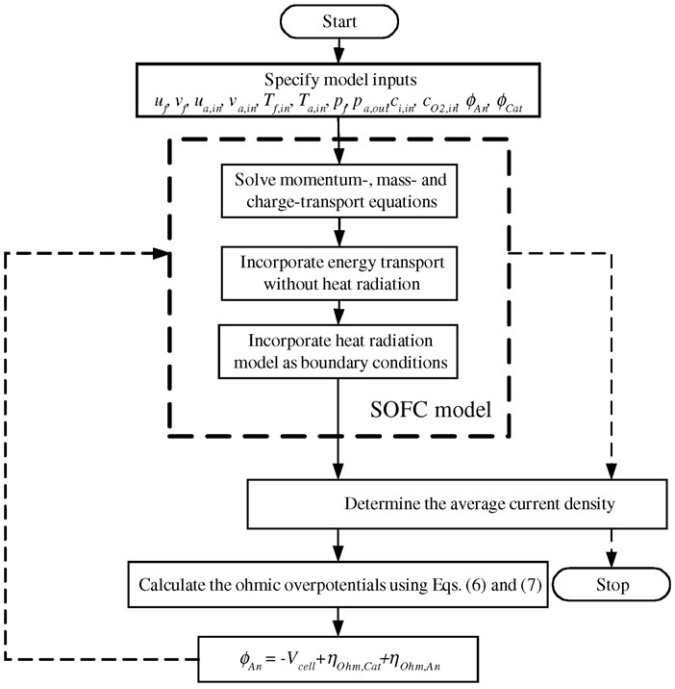

Fig. 3. Numerical algorithm for solution of the model equations.

2.3. Numerical implementation

Fig. 3 depicts the numerical algorithm to determine the cell performance curve for given inlet gas and cell operating conditions. ϕ_{Cat} is set to zero while ϕ_{An} is assigned to $-V_{cell}$. The finite-element FEMLAB® software package, version 3.1 [30] was used to solve the transport equations coupled with electrochemical reactions and the WGSR subject to the specified boundary conditions. The stationary nonlinear solver provided in the package was chosen for this purpose. Since the equations are highly nonlinear, it is very difficult to solve all governing equations simultaneously in a single step and so a three-step method was used. Once the model inputs including feed temperatures and pressures of fuel and air, species concentrations and operating cell voltage were specified, an isothermal version of the model including momentum, mass and charge transport was first solved. Afterwards, energy transport without radiation was incorporated into the existing model and re-run again using the results from the first step as initial guesses. Finally, the equation for radiative heat exchange was added to the boundary conditions as previously described and the results from the second run were used as initial guesses. We adopted a similar approach in our previous modelling study [19].

Once the current densities generated by H_2 and CO oxidation collected along the length of the anode were obtained from the model, the average current density J_{avg} was calculated according to the following equation:

$$J_{avg} = \frac{1}{L - L_{APT}}\int_{L_{APT}}^{L}(J_{H_2}(r_E, z) + J_{CO}(r_E, z))\,dz \quad (12)$$

J_{avg} was employed to estimate $\eta_{Ohm,Cat}$ and $\eta_{Ohm,An}$ using Eqs. (6) and (7). Then, ϕ_{An} was replaced by $\eta_{Ohm,Cat} + \eta_{Ohm,An} - V_{cell}$ and the SOFC model was re-run again using the new value of ϕ_{An} before J_{avg} and the cell voltage $V_{cell} = \phi_{Cat} - \phi_{An}$ were recalculated.

The FEMLAB software (v. 3.1), was run on a Pentium IV 2.6 GHz computer. The time required for each simulation was in the range of 25–50 min depending on the initial guesses for the state variables.

3. Results and discussion

3.1. Model validation

This model for syngas operation has been validated in the case of a button cell and the results are presented in a previous paper [13]. Experimental results and operating conditions reported in the paper by Hirano et al. [31] were used to validate the tubular SOFC model. The cell dimensions and operating conditions are listed in Table 2. The physical properties of cell components are adopted from Ref. [18].

Since the information provided by Hirano et al. [31] was not complete, we could validate our model using only the reported cell voltage, maximum cell temperature and outlet gas temperatures obtained at an average current density of 0.185 A cm^{-2}, as summarized in Table 3. Fuel and air flow rates were not reported

Table 2
Cell dimensions and operating conditions of a tubular SOFC tested by Hirano et al. [31]

Item	Symbol	Value
Cell dimensions		
Component thickness (μm)		
Air-preheating tube	–	1000
Supporting tube	–	1500
Cathode	–	700
Electrolyte	–	40
Anode	–	100
Diameter (mm)		
Inner side of the air-preheating tube	–	6.00
Outer side of the air-preheating tube	$2r_{APT}$	7.00
Inner side of the supporting tube	$2r_{AC}$	13.00
Outer side of the cathode	$2r_{C}$	14.40
Outer side of the electrolyte	$2r_{E}$	14.48
Outer diameter of the fuel channel	$2r_{FC}$	16.61
Length (mm)		
Air-preheating tube	L_{APT}	290
Cell	L	300
Operating conditions		
Fuel inlet conditions		
Pressure (atm)	$p_{f,in}$	1.0
Composition (mole fraction)		
H_2	y_{H_2}	0.557
H_2O	y_{H_2O}	0.277
CO	$y_{CO,in}$	0.108
CO_2	y_{CO_2}	0.058
Temperature (°C)	$T_{f,in}$	800.0
Air inlet conditions		
Pressure (atm)	$P_{a,in}$	1.0
Composition (mole fraction)		
O_2	$y_{O_2,in}$	0.21
N_2	$y_{N_2,in}$	0.79
Temperature (°C)	$T_{a,in}$	600.0
Other operating conditions		
Fuel utilization factor	U_f	0.80
O_2 utilization factor	U_a	0.25
Average current density (A m^{-2})	J_{avg}	1850

in Hirano et al. and they were adjusted in the model to attain $U_f = 0.80$ and $U_a = 0.25$ as given in Table 2.

From Table 3, the maximum deviation between experimental and model results is less than 5%. This demonstrates that the present model should be accurate enough for use in studying the cell behavior of a tubular SOFC operating with synthesis gas.

Table 3
Comparison between model results and experimental data from Hirano et al. [31]

Parameter	Result		Deviation (%)
	Experiment	Model	
Cell voltage (V)	0.715	0.69	~3.5
Maximum cell temperature (°C)	~1000	1021	~2.1
Maximum cell temperature location (mm)	140	120	
Gas outlet temperature (°C)	~860	840	~2.3
Fuel flow rate (kg h^{-1})	–	0.0091	–
Air flow rate (kg h^{-1})	–	0.081	–

3.2. Simulation results

This section aims at simulating the steady-state cell behavior of a tubular SOFC operating with humidified H_2 and a variety of synthesis gases as fuel. Particular focus is placed on the distributions of temperature, current density and species concentration within the cell and/or flow passages. The results from our previous modelling study [19] of a cell operating with humidified H_2 are also compared with those from the present analysis of operation using synthesis gases.

3.2.1. Base case input parameters

Table 4 lists the input parameter values for the base case used in this study. The cell configuration was adopted from Hagiwara et al. [32]. The gas feed compositions used in this study are given in Table 4. F1 fuel is humidified H_2 while F2, F3, F4 and F5 fuels are examples of various synthesis gases. F3 and F4 fuels are typical of biomass-derived synthesis gases obtained from air and oxygen gasifiers, respectively [14,17]. Since the methane content of these biomass syngas fuels is only 1–2% [14], the effect of methane steam reforming would be small. We, therefore, did not take CH_4 into consideration in the compositions of F3 and F4 reported in Table 4. Other operating parameters, except cell voltage, were also based on the work of Hagiwara et al. [32]. The operating cell voltage in this simulation was set at 0.7 V which is a typical value for SOFC operation. Fuel and air flow rates were computed to satisfy the specifications of fuel and air

Table 4
Operating conditions for the base case tubular SOFC model

Model inputs	Value
Cell geometry	Based on Hagiwara et al. [32]
Fuel inlet temperature (°C)	870
Air inlet temperature (°C)	600
Operating pressure (Pa)	1.0135×10^5
Air inlet composition (%)	21 O_2/79 N_2
Cell voltage (V)	0.7 V
Fuel utilization (%)	85
Air utilization (%)	16.7
Fuel inlet composition [14] (%)	
F1	97 H_2/3 H_2O/0 CO/0 CO_2/0 N_2
F2	20 H_2/3 H_2O/0 CO/14 CO_2/63 N_2
F3[a]	20 H_2/3 H_2O/20 CO/14 CO_2/43 N_2
F4[a]	32 H_2/3 H_2O/45 CO/15 CO_2/5 N_2
F5	20 H_2/3 H_2O/20 CO/0 CO_2/57 N_2
Fuel flow rates (m^3 h^{-1})	
F1	0.187
F2	0.467
F3	0.285
F4	0.155
F5	0.373

[a] Fuels F3 and F4 represent biomass-derived synthesis gases for air- and oxygen-blown gasification, respectively. These compositions were adapted from [2,17] where the concentration of methane was low (at most 2%). Consequently, the effect of methane was neglected in the present study.

utilization. The air flow rates did not vary much, between 0.6 and 0.8 $m^3\,h^{-1}$; the fuel flow rates are shown in Table 4.

3.2.2. Cell performance for various synthesis gas compositions

In this work, the performance of the solid oxide fuel cell is evaluated in terms of the power density and thermal efficiency. The thermal efficiency is calculated by using the equation:

$$\eta_{\text{thermal}} = \frac{P}{\Delta \text{H}_{\text{fuel}}} \times 100\% \quad (13)$$

where P and ΔH_{fuel} represent the electrical power generated by SOFC and enthalpy or thermal energy supplied at the fuel channel inlet, respectively. For an SOFC, ΔH_{fuel} using H_2 and CO as fuels is determined as

$$\Delta \text{H}_{\text{fuel}} = F_{\text{CO}}\,\text{LHV}_{\text{CO}} + F_{\text{H}_2}\,\text{LHV}_{\text{H}_2} \quad (14)$$

where LHV_{CO} and LHV_{H_2} are lower heating values for combustion of CO and H_2, respectively. F_{CO} and F_{H_2} are the molar flow rates of CO and H_2 fed into an SOFC, respectively.

Table 5 summarizes the power density, thermal efficiency, average cell temperature and thermal energy supplied to the cell of a cathode-supported tubular solid oxide fuel cell obtained using the different fuels. All reported values are for the same cell size, constant cell voltage and constant fuel and air utilization factors, as indicated in Table 4. Note that the volumetric flow rates and heating values of the fuels are given for a temperature corresponding to the fuel inlet temperature (870 °C). The fuel and air flow rates have been adjusted so that the fuel and air utilization factors remain at the values given in Table 4. This allows the thermal energy supplied to the cell (ΔH_{fuel}) to be calculated. As shown in Table 4, the fuel flow rate of the syngas fuels increases as the amount of H_2 and CO in the fuel decreases; the highest flow rate is required for F2 which contains only 20% H_2, while the lowest flow rate applied is for F4 which contains 32% H_2 and 45% CO. Fuels F3 and F5 are similar in terms of H_2 and CO content, but part of N_2 has been replaced by CO_2 in F3. The higher amount of inert nitrogen in F5 leads to higher flow rate requirement for F5 than for F3.

Table 5 shows that the power density increases as the energy content in the fuel (ΔH_{fuel}) increases. The cell power density using humidified H_2 (Fl) is about twice as high as that achieved using the synthesis gases while still maintaining higher thermal efficiency. The higher ΔH_{fuel} and lower required flow rate of humidified H_2 fuel enables the cell to reach an average operating temperature that is about 100 °C higher than in the other cases (Table 5). The higher cell temperature lowers both the associated overpotentials and internal cell resistances, thereby increasing both the power density and thermal efficiency. Note that the average temperature for all syngas fuels (F2 to F5) does not vary much and remains between 930 and 940 °C.

Table 5
Effect of synthesis gas compositions on tubular SOFC performance

Fuel	Power density ($W\,m^{-2}$)	Thermal efficiency (%)	Average cell temperature (°C)	ΔH_{fuel} ($J\,s^{-1}$)
F1	2450	53.8	1040	133
F2	1073	46.5	929	69
F3	1203	39.9	940	90
F4	1242	38.8	935	95
F5	1433	36.3	933	117

Among the various synthesis gases, the lowest power density is obtained from the F2 fuel because it contains a small amount of H_2 with only CO_2 and N_2 diluents. Another reason for the lower power density of F2 is that some of the CO_2 reacts with H_2 to form H_2O and CO via the reverse WGSR, which lowers the reversible cell voltage. Replacement of some of the N_2 in F2 by CO in making up F3 fuel (20% CO) increases the power density from 1073 to 1203 $W\,m^{-2}$ because ΔH_{fuel} is higher for F3 than for F2. In addition, the extent of the reverse gas shift reaction is not as important in the case of F3 and so tends to increase the reversible cell voltage compared to F2. F5 fuel yields the highest power density of the synthesis gases since it has the highest ΔH_{fuel} and initially contains no CO_2. Comparison of the results for F3 and F5 shows that the presence of CO_2 has a negative effect on the power density (1203 $W\,m^{-2}$ for F3 and 1433 $W\,m^{-2}$ for F5). The presence of CO_2 in the synthesis gas decreases the cell power density because it not only reduces the reversible cell voltage but also the electrochemical reaction rate due to its reaction with H_2 to produce CO and H_2O via the reverse WGSR. Fuel F4 contains the largest concentrations of oxidizable species among the syngas compositions (77% of F4 is H_2 and CO). Thus, a smaller flow rate is required to achieve 85% fuel utilization, resulting in ΔH_{fuel} being slightly higher than for F3, but lower than F5. The power density of F4 lies, therefore, between that of F3 and F5.

In the present simulations, the fuel and air utilizations were kept constant and the flow rates of fuel and air were varied accordingly, resulting in different rates of enthalpy supplied to the cell (ΔH_{fuel}) from one fuel to the other. The power density appears to show a strong correlation with ΔH_{fuel}. One should be careful, however, not to conclude too quickly that the higher the concentration of H_2 and CO in the syngas, the higher ΔH_{fuel} and thus the higher the power density at constant fuel and air utilization factors. Although this is true for fuels F2, F3 and F4, it is not the case for F5. F5 has similar concentrations of H_2 and CO as F3, and lower concentrations of these two gases than F4; yet, because its flow rate is larger than for F3 and F4, ΔH_{fuel} for F5 is actually higher, leading to a higher power density. An important difference between F5 and the other syngas fuels is that it is the only fuel for which the water gas shift reaction will occur spontaneously in the forward direction. The reaction quotients $[P_{\text{CO}_2} P_{\text{H}_2}/(P_{\text{CO}} P_{\text{H}_2\text{O}})]$ for F2, F3 and F4 are well above the equilibrium constant at 870 °C and thus the reverse water gas shift reaction will occur spontaneously. The negative effect of the reverse water gas shift reaction is two-fold in the present simulation: (1) it reduces the reversible cell voltage compared to what would be obtained if it did not occur and (2) it consumes H_2 and produces CO. Since the simulations were performed at constant fuel utilization factor and since the rate of CO electrochemical oxidation is two to three times less than that of H_2 [13,33], the reverse WGS reaction leads to a decrease in power den-

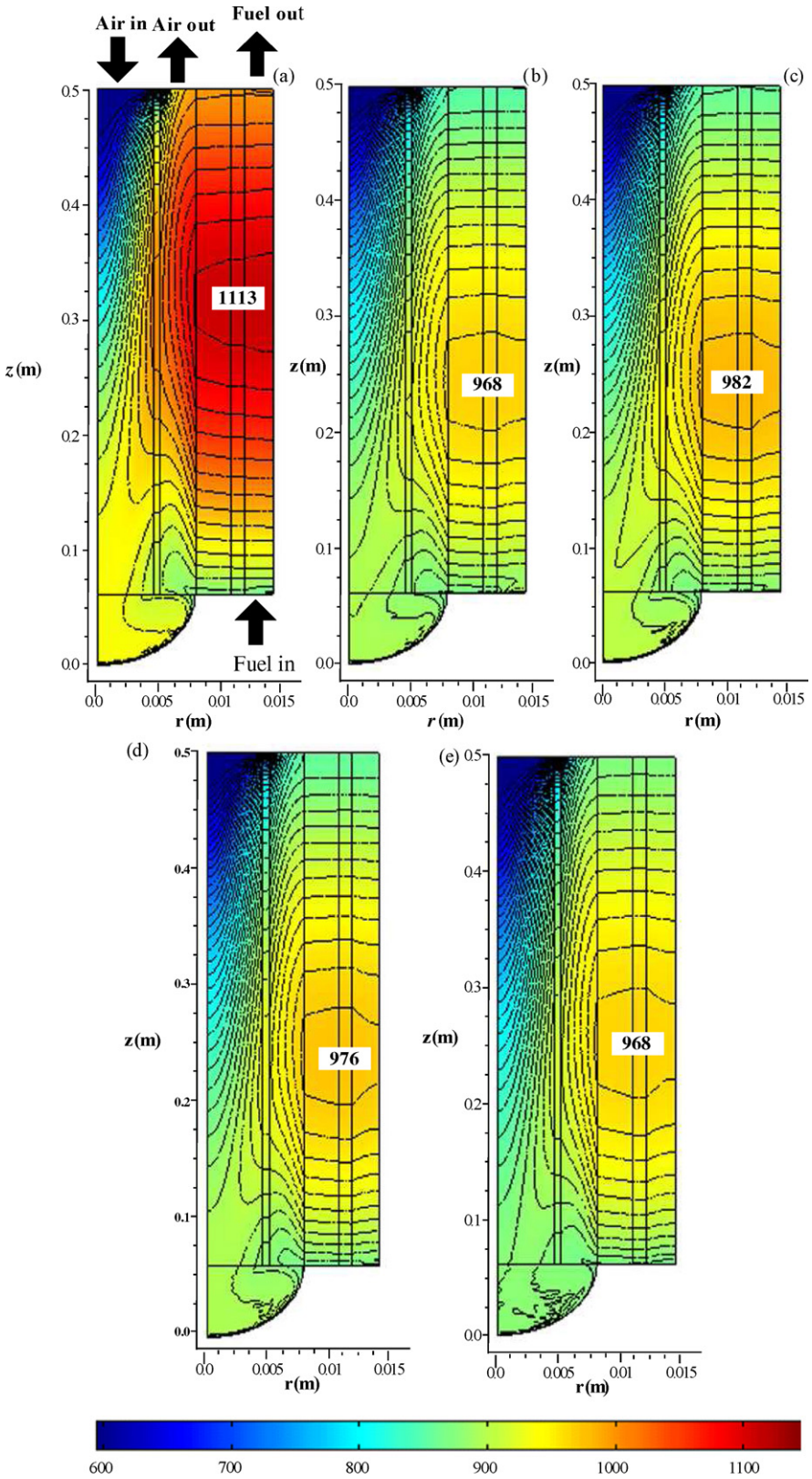

Fig. 4. Temperature fields for the base case model using Fl composed of humidified H_2 (a) and various synthesis gases F2 (b), F3 (c), F4 (d) and F5 (e) as fuel sources. Their compositions are given in Table 4.

sity compared to what would be obtained in the absence of this reaction.

Since this study focuses only on a single tubular cell, the thermal efficiency presented is based on the enthalpy of the fuel stream at the cell inlet temperature (870 °C). Therefore, the reported efficiency does not take into account any pre-heating of the fuel to 870 °C and air to 600 °C. It does, however, consider heating of air as it flows through the pre-heating tube. The thermal efficiency here simply represents the fraction of energy supplied at the fuel inlet that is converted into electricity. Table 5 shows that the variation in the thermal efficiency for the syngas fuels (F2 to F5) has the opposite trend to that of ΔH_{fuel} and the power density. The cell efficiency using the F2 fuel is much higher than those obtained using the other synthesis gases (F3 to F5). As shown in Table 5, the thermal efficiency is reduced from 46.5 to 39.9%, when the synthesis gas is changed from F2 to F3. When replacing F2 by F3, both ΔH_{fuel} and the power density increase, but the increase in ΔH_{fuel} (30% increase) is greater than that of the power density (12% increase), resulting in a decrease in thermal efficiency (see Eq. (13)). The observation that the relative increase in ΔH_{fuel} is greater than that of the power density appears to hold for all syngas fuels. Note that this is valid only for the syngas compositions considered in the present study. For humidified hydrogen (fuel Fl), both the power density and the thermal efficiency are greater than that of any of the syngas fuels.

Finally, analysis of the results for the two biomass-derived syngas fuels (F3 and F4), shows that the power density for oxygen-blown gasification (F4) increases by only 3% compared to that for the air-blown gasifier (F3). The difference in cell thermal efficiency is also less than 3%. Considering these small differences, it seems that air-blown gasification is adequate if the syngas is to be used in an SOFC. Note, however, that the flow rate required for the oxygen-blown syngas to achieve the target air and fuel utilization is only slightly more than half that of the air-blown gas.

3.2.3. Temperature distribution

Fig. 4 shows the temperature fields within the tubular cell using humidified H_2 and the various synthesis gases as fuel sources. Not surprisingly, the temperature dramatically increases as the air enters and makes its way through the air-preheating tube due to the large amount of heat transferred from the cell structure to the incoming fresh air. In each case, the cell temperature is at a maximum in the vicinity of the centre of the cell.

A comparison of the temperature profiles obtained for humidified H_2 to those for the synthesis gases shows that the maximum cell temperature for the former case is ~130 °C greater than for the others due to the higher thermal energy yield. Although operation at a higher temperature may have some potential advantages for cell performance, it also poses the risk of damaging the fuel cell due to the high temperature gradients that can be generated. This implies that an important advantage of using synthesis gases to power a TSOFC is better heat management and possibly more stable cell operation.

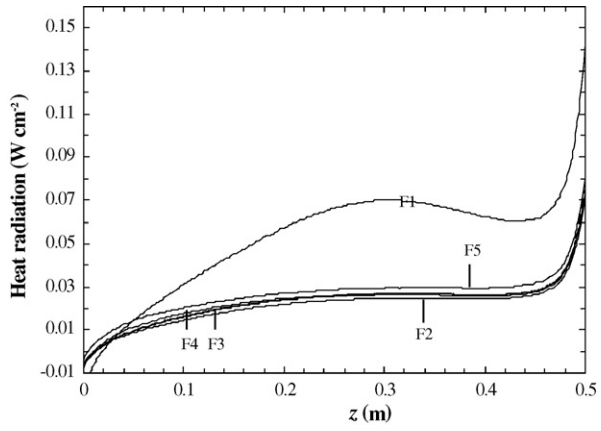

Fig. 5. Variation in the rate of radiative heat transport from the cathode surface ($r = r_{\text{AC}}$) to the wall surface of the air-preheating tube along the axial direction. The zero on the x-axis of this figure represents the origin taken at $z = L_{\text{APT}}$.

Fig. 5 shows the variation in the rate of heat radiated from the cathode surface to the wall surface of the air pre-heating tube for cells operating with gases Fl–F5. The rate of heat radiation is much greater for Fl than for the other gas streams because humidified H_2 electrochemically generates a higher amount of heat than synthesis gas. As shown in Fig. 5, radiative heat is transferred back from the air-preheating tube to the cathode surface and so has a small negative value (~−0.01 W cm^{-2}) near the fuel inlet at $z = 0$ since the temperature of the air-preheating tube is slightly greater than that at the cathode surface at this point within the cell. As one moves away from the fuel inlet, the rates of heat radiation increase until a location of $z \sim 0.30$ m is reached in the case of Fl and $z \sim 0.2$ m is reached for F2–F5. Thereafter, the radiation rate in the case of humidified H_2 decreases slightly from ~0.07 to ~0.055 W cm^{-2} before dramatically increasing from ~0.055 to ~0.14 W cm^{-2} from $z \sim 0.45$ to $z = 0.5$ m due to the large amount of heat radiated to the incoming fresh air. In contrast, the radiation rates in the case of the synthesis gases remain uniform at ~0.02 W cm^{-2} from $z \sim 0.2$ to $z \sim 0.45$ m before dramatically increasing from ~0.03 to ~0.08 W cm^{-2} over the final 0.05 m of the cell.

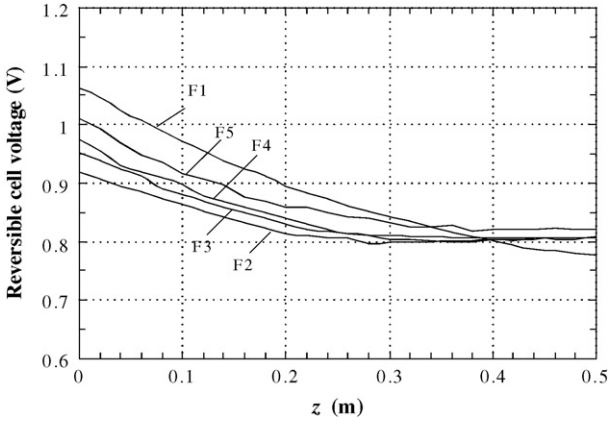

Fig. 6. Distributions of the reversible cell voltages along the cell length for operation with humidified H_2 and synthesis gases.

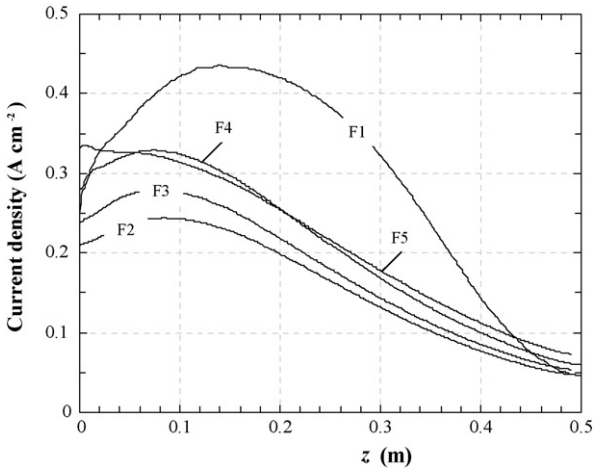

Fig. 7. Distribution of current density along the cell length for operation with humidified H_2 and the synthesis gases.

3.2.4. Distributions of reversible cell voltage, overpotential and current density

Fig. 6 illustrates the distributions of the reversible cell voltages (E^0) along the axial direction for humidified H_2 and the synthesis gases. It is important to note here that E^0 for the case of synthesis gas is determined by averaging E^0_{CO} and $E^0_{H_2}$. E^0 for the case of humidified H_2 is higher than those attained in the presence of the synthesis gases at the fuel inlet region because of higher reactant (or fuel) concentration (H_2 is the only reactant for the case of F1 while a H_2/CO mixture is the reactant for the case of F2 to F5). Further along the axial direction, E^0 in the case of humidified H_2 decreases until it becomes lower than that of the synthesis gases at $z \sim 0.4$ m because of the depletion of fuel and oxidant. Although the fuel temperature decreases at the fuel outlet (see Fig. 4) which should enhance E^0, it still continues to decline in this region because the effect of fuel and oxidant depletion on E^0 in this case is stronger than that of temperature reduction. The trend in the case of synthesis gases is similar in that E^0 decreases over the region from $z = 0$ to $z \sim 0.3$ m before stabilizing at a constant value near the fuel outlet. It seems that the influence of fuel and oxidant depletion that causes a reduction in E^0 is counterbalanced by an increase in E^0 due to lower temperature. Fig. 7 displays the distributions of current densities along the cell length for humidified H_2 and the synthesis gases. In most cases, the current density increases as one moves away from the fuel inlet and reaches a maximum before decreasing as the outlet is approached. The high fuel concentration at the inlet results in a high reaction rate in this portion of the cell. The current density continues to increase further along the cell length although the fuel concentration begins to decrease due to the increase in the local cell temperature (Fig. 4). Thus, the position of maximum current density is located further downstream than the position of maximum fuel concentration. Beyond this point, the current density starts to decrease while the local temperature is still increasing since the influence of fuel depletion now becomes dominant.

The distributions of the cathodic and anodic overpotentials along the cell length are shown in Fig. 8. It is clearly seen that

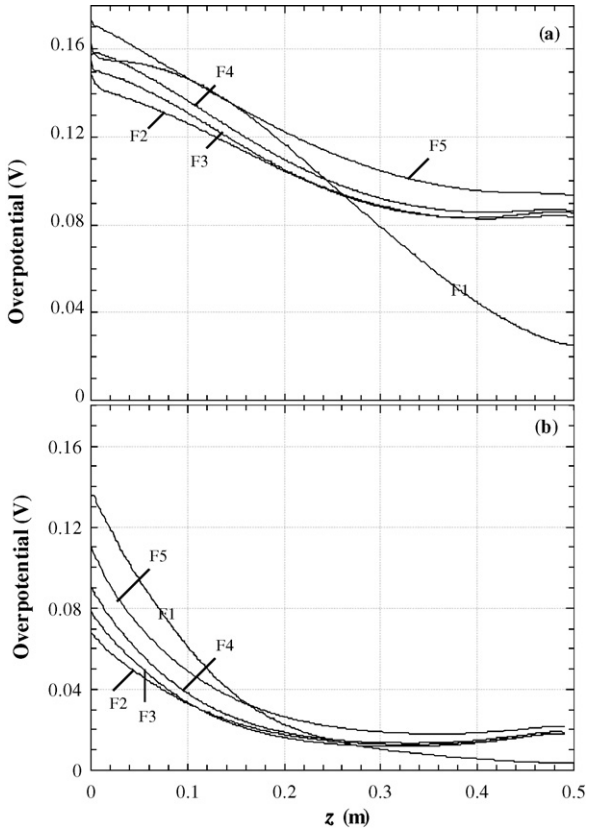

Fig. 8. Distributions of cathodic (a) and anode (b) overpotential along the cell length operation with humidified H_2 and synthesis gases.

the magnitude of the cathodic overpotential is larger than that of the anodic overpotential. This is due to the inherently slower kinetics of the cathodic reaction than that of the anodic reactions. Furthermore, O_2 must diffuse through the thick porous cathode to reach the active sites at the cathode/electrolyte interface. The resulting depletion of O_2 at the active sites also tends to increase the overpotential.

From Fig. 8a, the cathodic overpotential in the case of humidified H_2 decreases slightly over the region from $z = 0$ to $z \sim 0.15$ m, but then decreases more rapidly toward the fuel outlet ($z = 0.5$ m). In the fuel inlet region, the increase in the cathodic overpotential due to the increase in current density is compensated by the decrease in the cathodic overpotential due to the concomitant increase in temperature (see Fig. 4). However, over the remainder of the cell, the steep reduction of the cathodic overpotential is mainly caused by the decrease in current density.

When a synthesis gas is used, the cathodic overpotential near the fuel inlet is similar to that obtained using humidified H_2. However, toward the cell outlet, the cathodic overpotential remains more or less constant in the case of the synthesis gases and higher than that for humidified H_2 although the corresponding current densities are similar to each other (see Fig. 7). This trend can be explained by the fact that the outlet cell temperatures in the case of the synthesis gases are lower than when humidified H_2 is used. Therefore, the effect of a decrease in current density is compensated by the effect of the decrease in local temperature.

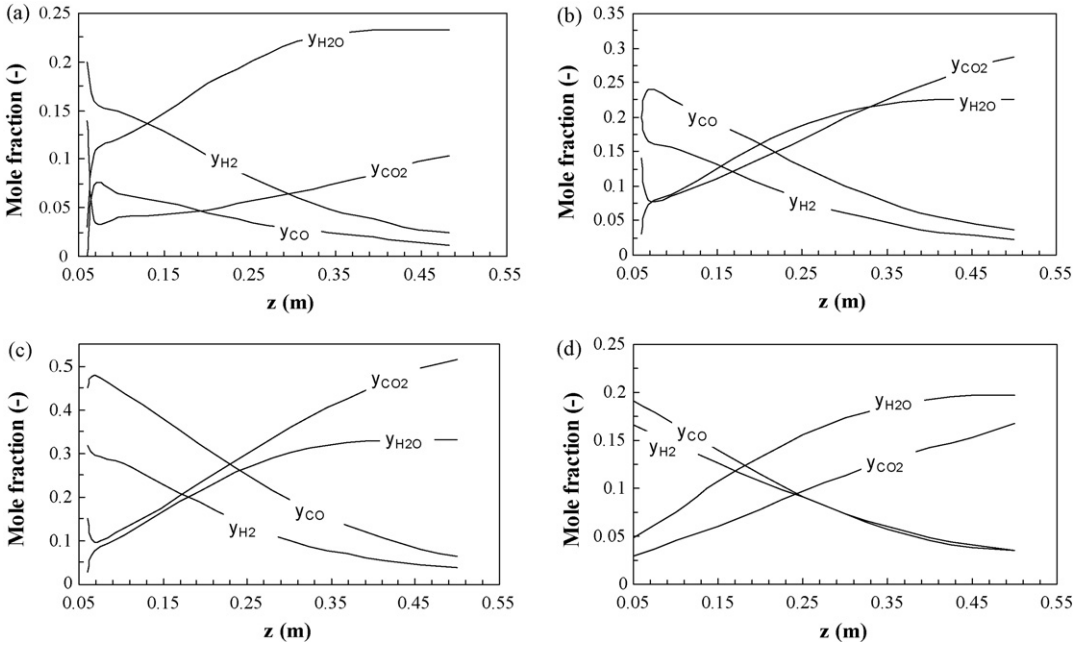

Fig. 9. Mole fractions of H_2, H_2O, CO and CO_2 along the fuel path for operation with synthesis gases F2 (a), F3 (b), F4 (c) and F5 (d).

Fig. 8b shows that the anodic overpotentials decrease significantly over the first half of the cell length. Beyond this point, the anodic overpotential for humidified H_2 decreases slightly, but increases slightly in the case of the synthesis gases for the same reasons as previously explained for the cathodic overpotential.

3.2.5. Distributions of species concentrations

Fig. 9 plots the distributions of the species concentrations along the cell length operating with gases F2 to F5. The species concentrations change sharply at the fuel inlet region because of the effect of the WGR adjusting them toward the equilibrium values based on the inlet compositions and fuel temperature. Thereafter, the H_2 and CO concentrations decrease while those of CO_2 and H_2O increase along the cell length due to the effect of the electrochemical reactions. It is worth noting that the rate of CO consumption is similar in magnitude to the rate of H_2 consumption although the electrochemical oxidation of CO is about two to three times slower than that of H_2 oxidation, as discussed

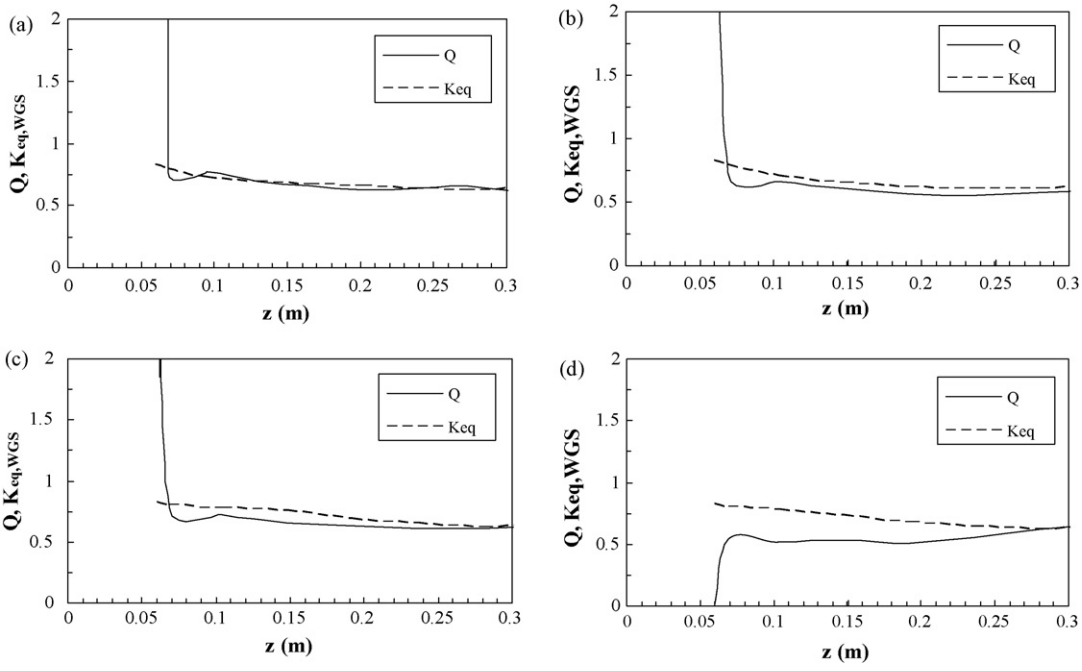

Fig. 10. Comparison of the reaction quotient and equilibrium constant for the water-gas shift reaction along approximately the first half of the fuel path for operation with synthesis gases F2 (a), F3 (b), F4 (c) and F5 (d).

previously [13,33]. The enhancement of the consumption rate of CO arises due to the effect of the WGSR whereby CO can also react with H_2O produced at the anode to form H_2 and CO_2. H_2 so formed is utilized by the electrochemical reaction again in the cycle. It is also observed that the rate of H_2 oxidation is higher than that of the WGR up to $z \sim 0.4$ m, as reflected by the increase in the molar fraction of H_2O.

An important objective of this work is to assess the validity of the common assumption that pseudo-equilibrium holds for the water-gas shift reaction within the reactor. From knowledge of the concentration of each species along the cell at the anode side (Fig. 9), the reaction quotient [$Q = P_{CO_2} P_{H_2}/(P_{CO}/P_{H_2O})$] can be determined at each location. If the reaction quotient is equal to the WGS equilibrium constant ($K_{eq,WGS}$), then pseudo-equilibrium has been reached. Comparison between Q and $K_{eq,WGS}$ along the cell length for each syngas fuel is shown in Fig. 10. This figure shows that Q approaches $K_{eq,WGS}$ very rapidly (within 1 cm) in the case of fuel F2. Thus, it is safe to assume equilibrium of the water-gas shift reaction everywhere along the fuel path for this fuel, which contains the lowest concentration of carbon oxides. For fuels F3 to F5, equilibrium is reached approximately 25 cm past the fuel path entrance, although the system is very close to equilibrium before this point in the case of the two biomass-derived syngases F3 and F4. For F5, the only fuel with a composition causing the inlet value of Q to be lower than $K_{eq,WGS}$, the difference between the reaction quotient and the equilibrium constant remains larger than for the other fuels, at least over the first 20 cm or so. This implies that the assumption of equilibrium for the WGS reaction for this fuel is not entirely valid, at least within a certain distance from the fuel inlet.

One should notice that the reaction quotient for F3, F4 and F5 along cell length is almost always lower than the equilibrium constant, even for the fuels for which the inlet Q was much greater than $K_{eq,WGS}$ (F3 and F4). This is likely related to the previous observation that the rate of H_2 oxidation is greater than that of the WGS reaction. Indeed, this leads to a higher concentration of water, thus lowering Q.

4. Conclusions

A mechanistic model of TSOFC using synthesis gas as a fuel source has been successfully developed and validated. The cell performance and its behavior obtained from the present model were compared with those obtained from our previous model [19] for a cell operating with humidified H_2. The model simulations indicate that the cell performance for operation with humidified H_2 is superior to that obtainable with the synthesis gases because higher average temperatures within the cell are reached due to the higher energy content of humidified H_2. For the syngas fuels, the cell average temperatures are about 100 °C lower than that of humidified hydrogen, resulting in lower temperature gradients within the cell. All syngas simulations were performed for constant air and fuel utilization factors and thus the fuel and air flow rates were adjusted accordingly leading to different values for the rate of enthalpy in the fuel stream (ΔH_{fuel}). Both the power density and thermal efficiency defined here as the fraction of the enthalpy rate of the fuel stream (inlet temperature conditions) converted into electric power appear to be closely related to ΔH_{fuel}. The power density rises and the thermal efficiency declines with an increase in ΔH_{fuel}. Important factors affecting ΔH_{fuel} are obviously the fuel composition and fuel flow rate, the latter being dependent on the fuel utilization factor. Our simulation results showed that the highest power density was achieved with a fuel with a composition favouring the forward direction of the water-gas shift reaction at the fuel inlet temperature. Lower power densities were achieved with fuels where the reverse water-gas shift reaction occurs. Again, this applies for the case of constant fuel utilization factor.

The use of two biomass-derived syngas fuels was investigated—one from air-blown gasification and the other from oxygen-blown gasification. The differences in power density and thermal efficiency between these two syngas fuels were small (less than 3%). The only major difference was that the flow rate of the oxygen-blown syngas was only slightly more than half that of the air-blown syngas to maintain 85% fuel utilization.

Finally, the results show that the assumption of WGS equilibrium is valid for fuels containing small amounts of carbon oxides (fuel F2). When the fuel (F3 and F4) has a composition such that the inlet reaction quotient is greater than the WGS equilibrium constant (i.e. the reverse WGS will initially occur spontaneously), the system was found to rapidly reach equilibrium, although the reaction quotient remains slightly below the equilibrium constant over the first half of the cell. In the case where the reaction quotient is initially lower then the equilibrium constant (F5), the system deviates further from equilibrium, at least over the first 20 cm of the fuel path.

Acknowledgements

Financial support from the Canadian Program for Energy Research and Development (PERD), CANMET CO_2 consortium and the Natural Sciences and Engineering Research Council of Canada (NSERC) is gratefully acknowledged.

References

[1] S.C. Singhal, Advances in solid oxide fuel cell technology, in: Proceedings of the 1998 Fuel Cell Seminar, Courtesy Associates, November 1998.
[2] A.O. Omosun, A. Bauen, N.P. Brandon, C.S. Adjiman, D. Hart, J. Power Sources 131 (2004) 96.
[3] K.D. Panopoulos, L.E. Fryda, J. Karl, S. Poulou, E. Kakaras, J. Power Sources 159 (2006) 570.
[4] S. Cordiner, M. Feola, V. Mulone, F. Romanelli, Appl. Therm. Eng. 27 (2007) 738.
[5] T. Aloui, K. Halouani, Appl. Therm. Eng. 27 (2007) 731.
[6] J. Van Herle, F. Marechal, S. Leuenberger, D. Favrat, J. Power Sources 118 (2003) 375.
[7] J. Van Herle, Y. Membrezb, O. Bucheli, J. Power Sources 127 (2004) 300.
[8] J. Van Herle, F. Marechal, S. Leuenberger, Y. Membrez, O. Bucheli c, D. Favrat, J. Power Sources 131 (2004) 127.
[9] S. Vasileiadis, Z. Ziaka-Vasileiadou, Chem. Eng. Sci. 59 (2004) 4853.
[10] C. Athanasiou, F. Coutelieris, E. Vakouftsi, V. Skoulou, E. Antonakou, G. Marnellos, A. Zabaniotou, Int. J. Hydrogen Energy 32 (2007) 337.
[11] Z. Xie, C. Xia, M. Zhang, W. Zhua, H. Wang, J. Power Sources 161 (2006) 1056.

[12] S. Baron, N. Brandon, A. Atkinson, B. Steele, R. Rudkin, J. Power Sources 126 (2004) 58.
[13] R. Suwanwarangkul, E. Croiset, S. Charojrochkul, M.W. Fowler, P.L. Douglas, E. Entchev, H. Mahaudom, S. Chewathanakup, J. Power Sources (2006) 308.
[14] P.V. Aravind, J.P. Ouweltjes, E. de Heer, N. Woudstra, G. Rietveld, in: S.C. Singhal, J. Mizusaki (Eds.), Proceeding of the 9th International Symposium on Solid Oxide Fuel Cells (SOFC-IX), The Electrochemical Society, 2005, p. 1459.
[15] T. Kaneko, J. Brouwer, G.S. Samuelsen, J. Power Sources 160 (2006) 316.
[16] J. Staniforth, K. Kendall, J. Power Sources 71 (1998) 275.
[17] A.V. Bridgwater, Fuel 74 (1995) 631.
[18] R. Suwanwarangkul, Model Development and Validation of Solid Oxide Fuel Cell Using H_2–H_2O–CO–CO_2 Mixtures: from Button Cell Experiments to Tubular and Planar Cells, Ph.D. Thesis, University of Waterloo, 2005, p. 264.
[19] R. Suwanwarangkul, E. Croiset, M.D. Pritzker, M.W. Fowler, P.L. Douglas, E. Entchev, J. Power Sources 154 (2006) 74.
[20] P.W. Li, K. Suzuki, J. Electrochem. Soc. 151 (4) (2004) A548.
[21] S. Nagata, A. Momma, T. Kato, Y. Kasuga, J. Power Sources 101 (2001) 60.
[22] P. Aguiar, D. Chadwick, L. Kershenbaum, Chem. Eng. Sci. 57 (2002) 1885.
[23] B. Bharadwaj, D.H. Archer, E.S. Rubin, J. Fuel Cell Sci. Technol. 2 (2005) 38.
[24] S. Campanari, P. Iora, J. Power Sources 132 (2004) 113.
[25] P.W. Li, M.K. Chyu, J. Heat Transfer 127 (2005) 1344.
[26] P.W. Li, M.K. Chyu, J. Power Sources 124 (2003) 487.
[27] G.K. Gupta, J.R. Marda, A.M. Dean, A.M. Colclasure, H. Zhu, R.J. Kee, J. Power Sources 162 (2006) 553.
[28] R. Suwanwarangkul, E. Croiset, M.W. Fowler, P.L. Douglas, E. Entchev, M.A. Douglas, J. Power Sources 122 (2003) 9.
[29] E.A. Avallone, T. Baumeister, Mark's Standard Handbook for Mechanical Engineers, 10th ed., McGraw Hill, New York, 1996.
[30] COMSOL Ltd., FEMLAB® Version 3.0 User's Guide, COMSOL, Boston, 2004.
[31] A. Hirano, M. Suzuki, M. Ipponmatsu, J. Electrochem. Soc. 139 (1992) 2744.
[32] A. Hagiwara, H. Michibata, A. Kimura, M.P. Jaszcar, G.W. Tomlins, S.E. S Veyo, Proceedings of the Third International Fuel Cell Conference, D2-4, 1999, p. 369.
[33] Y. Matzusaki, M. Hishinuma, I. Yasuda, in: S.C. Singhal, M. Dokiya (Eds.), Proceedings of Solid Oxide Fuel Cell VI, PV 99-19, The Electrochemical Society Proceedings Series, Pennington, NJ, 1999, p. 560.